A Terrain-Following Crystal Grid

Finite Volume Ocean Circulation Model

Peter C. Chu and Chenwu Fan

Naval Ocean Analysis and Prediction Laboratory

Department of Oceanography, Naval Postgraduate School

Monterey, CA 93943, USA

Abstract

A three dimensional hydrostatic finite volume ocean model is developed solving the integral dynamical equations. Since the basic (integral) equations are solved for finite volumes rather than grid points, the flux conservation is easily enforced even on arbitrarily meshes. Both upwind and high-order combine compact schemes can be incorporated into the model to increase computational stability and accuracy. For abrupt topography, a terrain-following grid discretization is designed to reduce computational errors such that the four lateral boundaries of each finite volume are perpendicular to x and y axes, and the two vertical boundaries are not purely horizontal. This grid system reveals a superior feature than z- and σ-coordinate systems. The accuracy of this model was tested in this study.

Key Words: Finite Volume, Crystal Grid, Integral Equations, Hydrostatic Balance, Terrain-Following Coastal Model.

1. Introduction

Four different schemes are available to solve partial differential equations numerically: (1) spectral or spectral transform, (2) finite difference, (3) finite element, and (4) finite volume. Because of the lateral boundaries with complicated shape, the ocean basin is inherently ill suited to the spectral technique. The finite element method has been applied to 2D barotropic problems extensively such as tides and storm surge (Foreman et al., 1993; Le Provost et al. 1994) due to the flexibility in adapting the grid locally to any desired resolution, but hasn't been applied to 3D baroclinic problems only until recent years (e.g., Lynch et al., 1996). A principal problem of this method appears to be the mass conservation. While globally this conservation is assured, it may not conserve the mass locally (Kantha and Clayson, 2000).

The finite difference method that transforms the partial differential equations into difference equations at grid points is commonly used in regional and basin-scale ocean modeling. Let (x, y) and z represent the horizontal and vertical directions. Various finite difference models use different vertical coordinates such as z-coordinate (e.g., Bryan, 1969), terrain following σ - and s-coordinates (e.g., Blumberg and Mellor, 1987; Song and Haidvogel, 1994), and isopycnal coordinate (Bleck et al., 1992). The solutions of the finite-difference models are valid only at the grid points. For coastal oceans, the finite-difference models usually use the terrain following σ-coordinate and have large truncation errors at steep topography that is caused by horizontal pressure gradient errors. Much work has been conducted to improve the accuracy of the σ-coordinate finite-difference models (e.g., Gary, 1973; Beckman and Haidvogel, 1993; Mellor et al., 1994; Chu and Fan, 1997, 1998, 1999, 2000, 2001).

The finite volume method that transforms the partial differential equations into integral equations at finite volumes has yet been popular in ocean circulation modeling and simulation.

However, the conservation is easily enforced even on arbitrary grids because the integral equations link the temporal variability of the dependent variables for the volume to the fluxes across the boundary of that volume (Kobayashi, 1999; Hermeline, 2000). This leads to the volume setup very flexible that makes the finite volume method invaluable especially in the abrupt topography.

In this paper, we present the formulation and preliminary test of the finite volume ocean model (VOM). The outline of this part is as follows: A description of the dynamic and thermodynamic integral equations is given in section 2. A depiction of the finite volume discretization with crystal grids, flux computation, and explicit finite volume scheme is given in sections 3. The preliminary model test case is depicted in section 4. The comparison between the finite difference and finite volume methods is discussed in section 5. In section 6, the conclusions are presented.

2. Dynamic and Thermodynamic Integral Equations

Let (x, y) and z be the horizontal and vertical Cartesian coordinates with the constant unit vectors ($\mathbf{e}_x$, e_y) and $\mathbf{e}_z$. The circulation model is established on the base of the two approximations: hydrostatic and anelastic. The anelastic approximation is to assume that the local time rate of change in density (ρ) is small; the continuity equation may be approximated by (Ogura and Phillips, 1962)

$$\nabla \bullet (\rho \mathbf{V}) = 0 . \tag{1}$$

Here, $\mathbf{V}$ = (u, v, w) is the velocity vector and ∇ is the three-dimensional gradient operator. The momentum equation is given by

$$\frac{\partial(\rho \mathbf{V})}{\partial t} + \nabla \bullet (\rho \mathbf{V}\mathbf{V}) = -\nabla p + \nabla \bullet (\mu \nabla \mathbf{V}) + \mathbf{F} , \tag{2a}$$

where p is the pressure, μ is the eddy viscosity. **F** represents the Coriolis force and gravity (body forces). Let ψ be a scalar representing temperature, salinity, satisfying the advection-diffusion equation

$$\frac{\partial \psi}{\partial t} + \nabla \bullet (\mathbf{V}\psi) = \nabla \bullet (\kappa_\psi \nabla \psi) + F_\psi , \tag{2b}$$

where κ_ψ and F_ψ are the mixing coefficient and the forcing term for ψ. The eddy viscosity and vertical mixing coefficients μ and κ_ψ using the level-2 turbulence closure (Mellor and Yamada, 1974).

Integration of (1) on a finite volume Ω (Fig. 1) leads to

$$\int_\Omega \nabla \bullet (\rho \mathbf{V}) d\Omega = \oint_\Gamma \rho \mathbf{V} \bullet \mathbf{n} d\Gamma , \tag{3}$$

and integration of (2a) and (2b) leads to

$$\int_\Omega \frac{\partial (\rho \mathbf{V})}{\partial t} d\Omega + \oint_\Gamma \rho \mathbf{V}\mathbf{V} \bullet \mathbf{n} d\Gamma = -\oint_\Gamma p\mathbf{n} d\Gamma + \oint_\Gamma \mu \nabla \mathbf{V} \bullet \mathbf{n} d\Gamma + \int_\Omega \mathbf{F} d\Omega , \tag{4a}$$

$$\int_\Omega \frac{\partial \psi}{\partial t} d\Omega + \oint_\Gamma \psi \mathbf{V} \bullet \mathbf{n} d\Gamma = \oint_\Gamma \kappa_\psi \nabla \psi \bullet \mathbf{n} d\Gamma + \int_\Omega F_\psi d\Omega , \tag{4b}$$

where Γ is the boundary of Ω and **n** is the unit vector normal to Γ (outward positive). The two equations (4a) and (4b) are quite similar in terms of using the finite volume method. The only difference is the pressure term, $-\oint_\Gamma p\mathbf{n} d\Gamma$. Equations (4a) and (4b) can be combined into one equation

$$\int_\Omega \frac{\partial \phi}{\partial t} d\Omega + \oint_\Gamma \phi \mathbf{V} \bullet \mathbf{n} d\Gamma = \oint_\Gamma \kappa_\phi \nabla \phi \bullet \mathbf{n} d\Gamma + \int_\Omega F_\phi d\Omega + \Delta P_\phi , \tag{4c}$$

where the scalar ϕ is one of $(\rho u, \rho v, \psi)$ and

$$\phi = \rho u, \quad \kappa_\phi = \mu, \quad \Delta P_\phi = \Delta P_x ,$$

$$\phi = \rho v, \quad \kappa_\phi = \mu, \quad \Delta P_\phi = \Delta P_y,$$

$$\phi = \psi, \quad \kappa_\phi = \kappa_\psi, \quad \Delta P_\phi = 0, \tag{5}$$

where $(\Delta P_x, \Delta P_y)$ are the (x, y) components of the pressure gradient force on the volume Ω.

For a temporally varying finite volume, the time rate of change of the volume integrated ϕ-value is computed by

$$\frac{\partial}{\partial t}\oint_\Omega \phi d\Omega = \oint_\Omega \frac{\partial \phi}{\partial t} d\Omega + \phi \frac{\partial \Omega}{\partial t}. \tag{6}$$

Substitution of (6) into (4c) leads to

$$\frac{\partial}{\partial t}\int_\Omega \phi d\Omega - \phi \frac{\partial \Omega}{\partial t} + \oint_\Gamma \phi \mathbf{V} \bullet \mathbf{n} d\Gamma = \oint_\Gamma \kappa_\phi \nabla \phi \bullet \mathbf{n} d\Gamma + \int_\Omega F_\phi d\Omega + \Delta P_\phi, \tag{7a}$$

which is the basic equation for ϕ (integral ϕ-equation). Time integration of (7a) from t_1 to t_2 gives

$$\int_\Omega \phi(t_2) d\Omega - \int_\Omega \phi(t_1) d\Omega = -\Delta t \oint_\Gamma \phi(t^*) \mathbf{V} \bullet \mathbf{n} d\Gamma$$

$$+\Delta t \oint_\Gamma \kappa_\phi \nabla \phi(t^*) \bullet \mathbf{n} d\Gamma + \Delta t \left[\int_\Omega F_\phi(t^*) d\Omega + \Delta P_\phi(t^*) \right] + \Delta t \left(\phi \frac{\partial \Omega}{\partial t} \right)_{t^*}, \tag{7b}$$

where $\Delta t = t_2 - t_1$, and $t_1 \le t^* \le t_2$. If $t^* = t_1$, the scheme is explicit; if $t^* = t_2$, the scheme is implicit. Adjustment of t^* may lead to a high-order temporal discrete scheme. The last term in the right-hand side of (7b) represents the temporal volume change due to surface elevation fluctuation.

3. Discretization

3.1. Terrain-Following Crystal Grids

Discretization of VOM in the horizontal directions

$$x = x(i), \quad y = y(j), \tag{8}$$

is similar to the z- and σ-coordinate systems. Discretization of VOM in the vertical direction,

$$z = z(i, j, k, t), \tag{9}$$

varies with the location (i, j, k) and time (t). Let the bottom topography is represented by

$$z = -H(x, y),$$

where $H(x, y)$ is assumed to be a singled value function of (x, y). Let $(\mathbf{e}_x, \mathrm{e}_y)$ be the constant unit vectors in the (x, y) directions.

Four types of finite volumes are constructed. Type-A (Fig. 1a) has four vertical lateral surfaces perpendicular to $\mathbf{e}_x$ or $\mathbf{e}_y$,

$$\mathbf{n}_x = \mathbf{e}_x, \quad \mathbf{n}_y = \mathbf{e}_y, \tag{10}$$

and the lower surface either away or at the ocean bottom. The four vertices (SW, NW, SE, NE) of the upper surface are away from the bottom topography. The upper and lower slanted surfaces are trapezoids. Type-B has one vertex of the upper surface at the bottom topography (say vertex SW). Since $H(x, y)$ is a single valued function, it is all land below the vertex SW. The lower surface of the finite volume is a triangle (no longer a trapezoid). Such a volume (Fig. 1b) still has four vertical surfaces and two slanted surfaces (both triangles). Type-C has two vertices of the upper surface at the bottom topography (say vertices SW and NW). It is all land below the vertices SW and NW. The lower surface shrinks into a line. The finite volume has two slanted surfaces and three vertical surfaces with two surfaces perpendicular to $\mathbf{n}_y$ and one surface perpendicular to $\mathbf{n}_x$ (Fig. 1c). Type-D has three vertices of the upper surface at the bottom topography with only one vertex (say NE) in the water. The vertices NW and SE are at the bottom boundary and the vertex SW is inside the land (not shown in Fig. 1d). The lower surface shrinks into a point. The finite volume has two slanted surfaces and two vertical surfaces perpendicular to $\mathbf{n}_x$ and $\mathbf{n}_y$ (Fig. 1d). This grid system is called the crystal grid due to the crystal shape of the finite volumes. The normal unit vector $(\mathbf{n}_s)$ on the slanted surfaces of all the four types of finite volumes is calculated by

$$\mathbf{n}_s = \left(-\frac{\partial z}{\partial x}\mathbf{n}_x - \frac{\partial z}{\partial y}\mathbf{n}_y + \mathbf{e}_z \right) / \sqrt{\left(\frac{\partial z}{\partial x}\right)^2 + \left(\frac{\partial z}{\partial y}\right)^2 + 1}\,. \tag{11}$$

The mesh characteristics make the VOM with crystal grid (Fig. 1) superior to the z- and σ-coordinate systems. Fig. 2 shows the discretization of VOM in the vertical direction differs from both z- and σ- coordinate models. The finite volumes with the crystal grids have six surfaces for non-boundary volumes and five surfaces for boundary volumes. To determine $\mathbf{n}_s$ in a finite volume enclosed by (x_i, x_{i+1}) in the x-direction and by (y_j, y_{j+1}) in the y-direction, a bi-linear interpolation is used to obtain the s-boundary (i.e., slanted boundary) for that volume,

$$z(x,y) = z_{11}\frac{(x-x_{i+1})(y-y_{j+1})}{(x_i-x_{i+1})(y_j-y_{j+1})} + z_{12}\frac{(x-x_{i+1})(y-y_j)}{(x_i-x_{i+1})(y_j-y_j)}$$

$$+ z_{21}\frac{(x-x_i)(y-y_{j+1})}{(x_{i+1}-x_i)(y_j-y_{j+1})} + z_{22}\frac{(x-x_i)(y-y_j)}{(x_{i+1}-x_i)(y_{j+1}-y_j)}, \tag{12}$$

where

$$z_{11} = z(x_i, y_j),\ \ z_{12} = z(x_i, y_{j+1}),\ \ z_{21} = z(x_{i+1}, y_j),\ \ z_{22} = z(x_{i+1}, y_{j+1})\,.$$

Substitution of (12) into (9) determines the unit vector $\mathbf{n}_s$ at the center of the horizontal cell, ($x_{i+1/2}$, $y_{j+1/2}$) = [($x_i + x_{i+1}$)/2, ($y_j + y_{j+1}$)/2],

$$\mathbf{n}_s = (\cos\theta_x,\ \cos\theta_y,\ \cos\theta_z)\,, \tag{13}$$

where

$$\cos\theta_x = -\frac{z_x(x_{i+1/2}, y_{j+1/2})}{\sqrt{1+z_x^2+z_y^2}},\quad \cos\theta_y = -\frac{z_y(x_{i+1/2}, y_{j+1/2})}{\sqrt{1+z_x^2+z_y^2}},\quad \cos\theta_z = \frac{1}{\sqrt{1+z_x^2+z_y^2}}$$

and $z_x \equiv \partial z/\partial x,\ \ z_y \equiv \partial z/\partial y$. The normal gradient of any variable ϕ is calculated by

$$\frac{\partial \phi}{\partial n_s} = \nabla\phi \bullet \mathbf{n}_s = \left(\frac{\partial \phi}{\partial z} - \frac{\partial \phi}{\partial x}z_x - \frac{\partial \phi}{\partial y}z_y \right) / \sqrt{1+z_x^2+z_y^2}\,. \tag{14}$$

3.2. Flux Computation

The surfaces of a finite volume perpendicular to ($\mathbf{n}_x$, $\mathbf{n}_y$, $\mathbf{n}_s$) are called the *x*-, *y*- and *s*-boundaries. In basic equations (4a) and (6), the fluxes across the *x*-boundary of a finite volume are computed by

$$f_m^x = \int_{x-boundary} \rho \mathbf{V} \bullet \mathbf{n}_x d\Gamma = \overline{\rho u} \Delta y \Delta z, \quad f_\phi^x = \int_{x-boundary} \phi \mathbf{V} \bullet \mathbf{n}_x d\Gamma = \overline{\phi u} \Delta y \Delta z ,$$

$$f_\tau^x = \int_{x-boundary} \kappa_\phi \nabla \phi \bullet \mathbf{n}_x d\Gamma = \overline{\kappa_\phi \frac{\partial \phi}{\partial x}} \Delta y \Delta z, \;\; P_x^x = p \Delta y \Delta z, \;\; P_y^x = 0 , \qquad (15)$$

where the overbar indicates the spatially averaged value at the boundary surface, (P_x^x, P_y^x) are the two components of the horizontal pressure force on the *x*-boundary. The fluxes across the *y*-boundary of a finite volume are computed by

$$f_m^y = \int_{y-boundary} \rho \mathbf{V} \bullet \mathbf{n}_y d\Gamma = \overline{\rho v} \Delta x \Delta z, \quad f_\phi^y = \int_{y-boundary} \phi \mathbf{V} \bullet \mathbf{n}_y d\Gamma = \overline{\phi v} \Delta x \Delta z ,$$

$$f_\tau^y = \int_{y-boundary} \kappa_\phi \nabla \phi \bullet \mathbf{n}_y d\Gamma = \overline{\kappa_\phi \frac{\partial \phi}{\partial y}} \Delta x \Delta z, \;\; P_y^y = p \Delta x \Delta z, \;\; P_x^y = 0 . \qquad (16)$$

where (P_x^y, P_y^y) are the two components of the horizontal pressure force on the *y*-boundary. The fluxes across the *s-boundary* of a finite volume are computed by

$$f_m^s = \int_{s-boundary} \rho \mathbf{V} \bullet \mathbf{n}_s d\Gamma = \overline{\rho (w - u \frac{\partial z}{\partial x} - v \frac{\partial z}{\partial y})} \Delta x \Delta y ,$$

$$f_\phi^s = \int_{s-boundary} \phi \mathbf{V} \bullet \mathbf{n}_s d\Gamma = \overline{\phi (w - u \frac{\partial z}{\partial x} - v \frac{\partial z}{\partial y})} \Delta x \Delta y ,$$

$$f_\tau^s = \int_{s-boundary} \kappa_\phi \frac{\partial \phi}{\partial n_s} d\Gamma = \overline{\kappa_\phi (\frac{\partial \phi}{\partial z} - \frac{\partial \phi}{\partial x}\frac{\partial z}{\partial x} - \frac{\partial \phi}{\partial y}\frac{\partial z}{\partial y})} \Delta x \Delta y ,$$

$$P_x^s = -p \frac{\partial z}{\partial x} \Delta x \Delta y, \;\; P_y^s = -p \frac{\partial z}{\partial y} \Delta x \Delta y , \qquad (17)$$

where (P_x^s, P_y^s) are the two components of the horizontal pressure force on the *s*-boundary. It is noticed that the derivatives should be computed by

$$\frac{\partial \phi}{\partial x} = \frac{\delta \phi}{\delta x} - \frac{\partial z}{\partial x}\frac{\delta \phi}{\delta z}, \quad \frac{\partial \phi}{\partial y} = \frac{\delta \phi}{\delta y} - \frac{\partial z}{\partial y}\frac{\delta \phi}{\delta z}, \quad \frac{\partial \phi}{\partial z} = \frac{\delta \phi}{\delta z}, \tag{18}$$

where ($\delta\phi/\delta x,\ \delta\phi/\delta y,\ \delta\phi/\delta z$) are computed directly from the grid point data.

3.3. Explicit Scheme

The finite volume scheme for solving continuity equation (3) at (i, j, k) is

$$f_m^x(i+\frac{1}{2}, j, k) - f_m^x(i-\frac{1}{2}, j, k) + f_m^y(i, j+\frac{1}{2}, k) - f_m^y(i, j-\frac{1}{2}, k)$$

$$+ f_m^s(i, j, k+\frac{1}{2}) - f_m^s(i, j, k-\frac{1}{2}) = 0\,. \tag{19}$$

The finite volume scheme for solving the basic equation (7b) is explicit if $t^* = t_1$,

$$[\phi_{i,j,k}^{(n+1)} - \phi_{i,j,k}^{(n)}]\Omega_{i,j,k} = f_\phi^x(i-\frac{1}{2}, j, k) - f_\phi^x(i+\frac{1}{2}, j, k) + f_\phi^y(i, j-\frac{1}{2}, k) - f_\phi^y(i, j+\frac{1}{2}, k)$$

$$+ f_\phi^s(i, j, k-\frac{1}{2}) - f_\phi^s(i, j, k+\frac{1}{2}) - f_\tau^x(i-\frac{1}{2}, j, k) + f_\tau^x(i+\frac{1}{2}, j, k) - f_\tau^y(i, j-\frac{1}{2}, k)$$

$$f_\tau^y(i, j+\frac{1}{2}, k) - f_\tau^s(i, j, k-\frac{1}{2}) + f_\tau^s(i, j, k+\frac{1}{2}) + F(i, j, k)\Omega_{i,j,k} + \Delta P_\phi(i, j, k) + \Delta t\left(\phi\frac{\partial \Omega}{\partial t}\right)_{i,j,k}^{(n)}, \tag{20}$$

where n is the time step. The upper-most finite volumes ($k = 1$) $\Omega_{i,j,1}$ changes with time when the surface elevation η varies,

$$\left(\frac{\partial \Omega}{\partial t}\right)_{i,j,1}^{(n)} = \Delta x \Delta y \left(\frac{\partial \eta}{\partial t}\right)_{i,j}^{(n)},$$

The finite volumes below the surface $\Omega_{i,j,k}$ ($k > 1$) do not change with time,

$$\left(\frac{\partial \Omega}{\partial t}\right)_{i,j,k}^{(n)} = 0, \qquad \text{for } k \neq 0\,.$$

The horizontal pressure gradient force ($\Delta P_x, \Delta P_y$) on the finite volume is computed by

$$\Delta P_x = P_x^x(i-\frac{1}{2}, j, k) - P_x^x(i+\frac{1}{2}, j, k) + P_x^s(i, j, k-\frac{1}{2}) - P_x^s(i, j, k+\frac{1}{2}), \tag{21}$$

$$\Delta P_y = P_y^y(i, j-\frac{1}{2}, k) - P_y^y(i, j+\frac{1}{2}, k) + P_y^s(i, j, k-\frac{1}{2}) - P_y^s(i, j, k+\frac{1}{2}). \tag{22}$$

4. Preliminary Test

4.1. Test Strategy

Usually, verification of a new numerical model should be divided into stages: (1) evaluating its own performance, and (2) identifying its difference from the existing models. Theoretically, the performance of any numerical ocean model should only be tested against analytical or known solutions. For coastal ocean, it hardly finds any analytical solutions. Known solution is hard to find. Without atmospheric and lateral forcing, the ocean that is initially at rest should be at rest forever. Thus, we have the known solutions for this case,

$$\mathbf{V} = 0, \quad \frac{\partial p}{\partial x} = 0, \quad \frac{\partial p}{\partial y} = 0. \tag{23}$$

The seamount test case (Beckmann and Haidvogel, 1993) is to use this known solution for model evaluation. Any nonzero horizontal pressure gradients (or velocities) obtained from the numerical model are considered errors.

Several advanced test cases have been proposed to identify the model-model difference and the sensitivity to the choice of (say) advection algorithm, such as gravitational adjustment of density front, residual circulation over a coastal canyon, combined effects of topography and stratification (Haidvogel and Beckmann, 1998). The second stage test should be conducted after the first stage test. In this paper, we only present the first stage evaluation using the seamount test case.

In regional oceanic (or atmospheric) prediction models, the effects of bottom topography must be taken into account and usually the terrain-following sigma coordinates should be used to imply the continuous topography. In sigma coordinates the water column is divided into the same number of grid cells regardless of the depth. Consider 2D problems for mathematical simplification. Let (x, z) be the Cartesian coordinates and ($\hat{x}$, σ) be the sigma coordinates. The conventional relationships between z- and σ-coordinates are given by

$$\hat{x} = x, \qquad \sigma = \frac{z-\eta}{H+\eta}, \tag{24}$$

where η is the surface elevation. Both z and σ increase vertically upward such that $z = \eta$, $\sigma = 0$ at the surface and $\sigma = -1$, z = -H at the bottom. The horizontal pressure gradient becomes difference between two large terms

$$\frac{\partial p}{\partial x} = \frac{\partial \hat{p}}{\partial \hat{x}} - \frac{1}{H+\sigma}\left(\sigma\frac{\partial H}{\partial \hat{x}} + \frac{\partial \eta}{\partial x}\right)\frac{\partial \hat{p}}{\partial \sigma}, \tag{25}$$

that may cause large truncation error at steep topography (e.g., Gary 1973; Haney 1991; Mellor et al. 1994; McCalpin 1994; Chu and Fan, 1997, 1998, 1999, 2000, 2001, 2003; Song 1998). Since the horizontal pressure gradient error is a key problem in the terrain-following ocean models, the first step of the VOM test should be the evaluation of its capability on reducing the horizontal pressure gradient error.

4.2. Seamount Test Case

Suppose a seamount located inside a periodic f-plane ($f_0 = 10^{-4}$ s^{-1}) channel with two solid, free-slip boundaries along constant y. Unforced flow over seamount in the presence of resting, level isopycnals is an idea test case for the assessment of pressure gradient errors in simulating stratified flow over topography. The flow is assumed to be reentrant (periodic) in the along channel coordinate (i.e., x-axis). The seamount test case is chosen to test the performance of VOM.

The domain is a periodic channel, 300 km long and 300 km wide. The channel has a far-field depth $h_{\max}$ and in the center includes an isolated Gaussian-shape seamount with a width L and an amplitude $\alpha h_{\max}$ (Fig. 3),

$$h(x,y) = h_{\max}\left\{1-\alpha\exp\left[-\frac{(x-x_0)^2+(y-y_0)^2}{L^2}\right]\right\}, \tag{25}$$

where (x_0, y_0) are the longitude and latitude of the seamount center. In this study, we use

$$h_{\max} = 4500 \text{ km},\ L = 25 \text{ km},\ \alpha = 0.9\,. \tag{26}$$

Suppose that the background fluid is at rest and with a constant salinity (35 ppt) and an exponentially stratified initial temperature,

$$T(z) = 5 + 15\exp(\frac{z}{H_T}) \qquad (\text{unit: } {}^{o}C)\,, \tag{27}$$

where H_T = 1000 m. Since the fluid is initially at rest and the density field is independent on x and y, without forcing the velocity and horizontal pressure gradient should be zero. Any nonzero velocities are computational errors.

4.3. Experiment Setting

A σ-coordinate finite difference model, the Princeton Ocean Model (POM, Blumberg and Mellor, 1987), is implemented for the seamount test case using horizontally varying grids with high resolution over the seamount,

$$(\Delta x)_i = 8 \text{ km}\left[1-0.5\sin\left(\frac{i\pi}{M_x}\right)\right], \quad i = 1,2,...,M_x\,,$$

$$(\Delta y)_j = 8 \text{ km}\left[1-0.5\sin\left(\frac{j\pi}{M_y}\right)\right], \quad \mathrm{j} = 1,2,...,M_y\,. \tag{28}$$

where $M_x = M_y = 64$. The VOM with the same physics, parameterization, and horizontal grids as the POM is also implemented for seamount test case. The vertical cross-sections of the VOM and POM are illustrated in Figs. 2b and 2c. The time steps for barotropic and baroclinic modes are 6 s and 180 s, respectively.

5. Comparison of Finite Difference and Finite Volume Schemes

5.1. Temporal Variations of Error Volume Transport

Both cases are integrated for 20 days for the standard test. Fig. 4 displays errors in the volume transport streamfunction after performing 20 days of integration using the finite volume and finite difference schemes. The volume transport streamfunction has a large-scale eight-lobe pattern centered on the seamount. The errors in the volume transport reduce more than 50% from finite difference to finite volume schemes. On the 20th day, the errors in the volume transport varies from -56 to 84×10^{-3} Sv using the POM and from -28 to 45.5×10^{-3} Sv using the VOM.

5.2. Temporal Variations of Pressure Gradient Error

Owing to a very large number of calculations performed, we discuss the results exclusively in terms of the maximum and spatially averaged absolute values of the horizontal pressure gradient errors, called the maximum pressure gradient error (PG_{max}) and the mean pressure gradient error (PG_m). Figure 5a and 5b show the time evolution of PG_{max} and PG_m for the first 20 days of integration using the finite difference and finite volume schemes. Both errors increase with time, however, they are 10-15 times smaller using the finite volume scheme than using the finite difference scheme. For example, at Day-10, $PG_{max} = 33.42\times10^{-9}$ N/m^3 using the finite difference scheme and $PG_{max} = 2.16\times10^{-9}$ N/m^3 using the finite volume scheme; $PG_m = 0.449\times10^{-9}$ N/m^3 using the finite difference scheme and $PG_m = 0.04\times10^{-9}$ N/m^3 using the finite volume scheme; at Day-20, $PG_{max} = 58.41\times10^{-9}$ N/m^3 using the finite difference scheme and $PG_{max} = 4.18\times10^{-9}$ N/m^3

using the finite volume scheme; $PG_m = 1.596 \times 10^{-9}$ N/m^3 using the finite difference scheme and $PG_m = 0.150 \times 10^{-9}$ N/m^3 using the finite volume scheme.

5.3. Temporal Variations of Error Velocity

Owing to a very large number of calculations performed, we discuss the results exclusively in terms of the maximum and spatially averaged absolute values of the spurious velocity generated by the pressure gradient errors, called the peak error velocity (V_p) and the mean error velocity (V_m). Figures 5c and 5d show the time evolution of the mean and peak error velocity for the first 20 days of integration using the finite difference and finite volume schemes. Both peak and mean error velocities increase with time, however, they are 4 times smaller using the finite volume scheme than using the finite difference scheme. For example, at Day-10, V_p = 2.61 cm/s using the finite difference scheme and V_p =0.57 cm/s using the finite volume scheme; V_m = 0.054 cm/s using the finite difference scheme and V_m =0.015 cm/s using the finite volume scheme; at Day-20, V_p= 4.25 cm/s using the finite difference scheme and V_p = 0.98 cm/s using the finite volume scheme; V_m = 1.033 cm/s using the finite difference scheme and V_m = 0.028 cm/s using the finite volume scheme.

6. Conclusions

(1) A three-dimensional, finite volume ocean circulation model has been developed. The basic equations are transformed from differential into integral forms using the hydrostatic and anelastic approximations and solved for finite volumes (rather than grid points) with the flux conservation enforced on arbitrarily meshes. This model has great flexibility in establishing model grids.

(2) A terrain-following grid discretization is proposed such that the vertical surfaces are perpendicular to horizontal (x, y) axes; and the slanted surfaces follow the ocean surface and

bottom. Such a grid system reveals a superior feature than both z- and σ-coordinate systems over abrupt bottom topography.

(3) Seamount test case is the first step to show the value-added of using finite volume scheme. The second-order finite volume scheme leads to a drastic error reduction comparing to the second-order finite difference scheme using POM.

(4) It is noticed that the seamount test case presented here is preliminary. More cases should be conducted in the future for testing the difference between VOM and the existing ocean models using gravitational adjustment of a density front, residual circulation over a coastal canyon, and combined effects of topography and stratification.

Acknowledgments

The authors wish to thank George Mellor and Tal Ezer of the Princeton University for most kindly providing us with a copy of the POM code. This work was funded by the Office of Naval Research, the Naval Oceanographic Office, and the Naval Postgraduate School.

References

Bleck, R., C. Roothe, D. Hu, and L. Smith (1992): Salinity-driven thermocline transients in a wind- and thermohaline-forced isopycnal coordinate model of the North Atlantic. *J. Phys. Oceanogr*., **22**, 1486-1505.

Blumberg, A.F., and G.L. Mellor (1987): A description of a three-dimensional coastal ocean circulation model. In: Three-Dimensional Coastal Ocean Models (edited by N. Heaps), pp. 1-16, Amer. Geophys. Union, Washington D.C..

Bryan, K. (1969): A numerical model for the study of the circulation of the world oceans. *J. Comput. Phys*., **4**, 347-359.

Chu, P.C., and C.W. Fan (1997): Sixth-order difference scheme for σ-coordinate ocean models. *J. Phys. Oceanogr*, 27, 2064-2071.

Chu, P.C., and C.W. Fan (1998): A three-point combined compact difference scheme. J. Comput. Phys., 140, 370-399.

Chu, P.C., and C.W. Fan (1999): A three-point sixth-order nonuniform combined compact difference scheme. J. Comput. Phys., 149, 1-12.

Chu, P.C., and C.W. Fan (2000): A three-point sixth-order staggered combined compact difference scheme. Math. Comput. Modeling, 32, 323-340.

Chu, P.C., and C.W. Fan (2001): An accuracy progressive sixth-order finite difference scheme. J. Atmos. Oceanic Technol., 18, 1245-1257.

Foreman, M.G.G., R.F. Henry, R.A. Walters, and V.A. Ballantyne (1993): A finite element model for tides and resonance along the north coast of British Columbia. J. Geophys. Res., 98, 2509-2532.

Haidvogel, D.B., and A. Beckmann (1997): Numerical modeling of the coastal ocean. The Sea, edited by K.H. Brink and A.R. Robinson, Vol 10, pp. 457-482, Wiley, New York.

Hermeline, F. (2000): A finite volume method for the approximation of diffusion operators on distorted meshes. J. Comput. Phys., 160, 481-499.

Kantha, L.H., and C.A. Clayson (2000): Numerical Models of Oceans and Oceanic Processes. Academic Press, San Diego, 940pp.

Kobayashi, M.H. (1999): On a class of Pade finite volume methods. J. Comput. Phys., 156, 137-180.

Le Provost, C., M.L. Genco, F. Lyard, P. Vincent, and P. Canceil (1994): Spectroscopy of the world tides from a finite element hydrodynamic model. J. Geophys. Res., 99, 24777-24797.

Lynch, D.R., J.T.C. Ip, C.E. Naimie, and F.E. Werner (1996): Comprehensive coastal circulation model with application to the Gulf of Maine. Cont. Shelf Res., 16, 875-906.

Mellor, G.L., T. Ezer, and L.-Y. Oey (1994): The pressure gradient conundrum of sigma coordinate ocean models. J. Atmos. Oceanic Technol., 11, 1 126-1 134.

Ogura, Y. and N.A. Phillips (1962): Scale analysis of deep and shallow convection in the atmosphere. J. Atmos. Sci., 19, 173-179.

Song, Y. and D.B. Haidvogel (1994): A semi-implicit ocean circulation model using a generalized topography-following coordinate. J. Comput. Phys., 115, 228-244.

Figure Legends

Fig. 1. Four types of finite volumes: (a) Type-A with four vertices (SW, NW, SE, NE) of the upper surface away from the bottom topography, (b) Type-B with one vertex (SW) of the upper surface at the bottom topography, (c) Type-C with two vertices (SW and NW) of the upper surface at the bottom topography, and (d) Type-D with three vertices of the upper surface at the bottom topography with only one vertex (NE) in the water.

Fig. 2. Comparison among (a) z-coordinate, (b) finite volume, and (c) σ-coordinate systems.

Fig. 3. Seamount geometry.

Fig. 4. Volume transport streamfunction (Sv) at day-20 using the finite difference and finite volume schemes.

Fig. 5. Comparison between the finite difference and finite volume schemes on temporal variations of (a) maximum pressure gradient error (N/m^3), (b) mean pressure gradient error (N/m^3), (c) peak error velocity (m/s), and (d) mean error velocity (m/s).

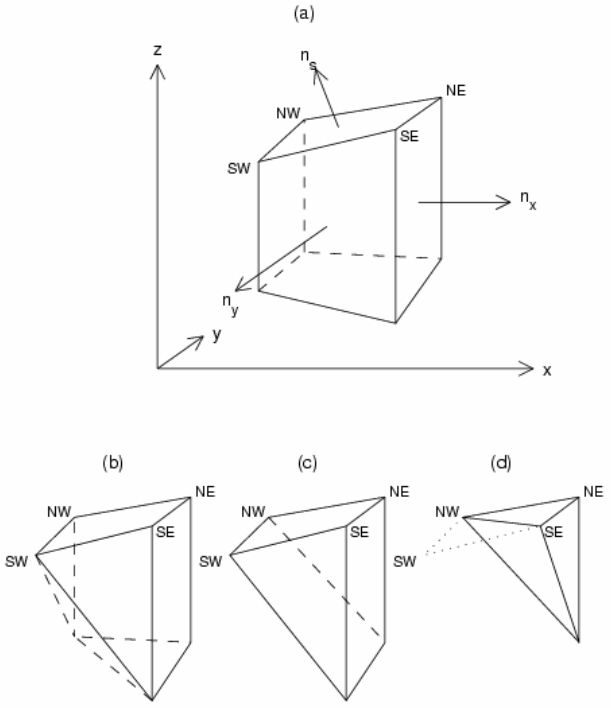

Fig. 1. Four types of finite volumes: (a) Type-A with four vertices (SW, NW, SE, NE) of the upper surface away from the bottom topography, (b) Type-B with one vertex (SW) of the upper surface at the bottom topography, (c) Type-C with two vertices (SW and NW) of the upper surface at the bottom topography, and (d) Type-D with three vertices of the upper surface at the bottom topography with only one vertex (NE) in the water.

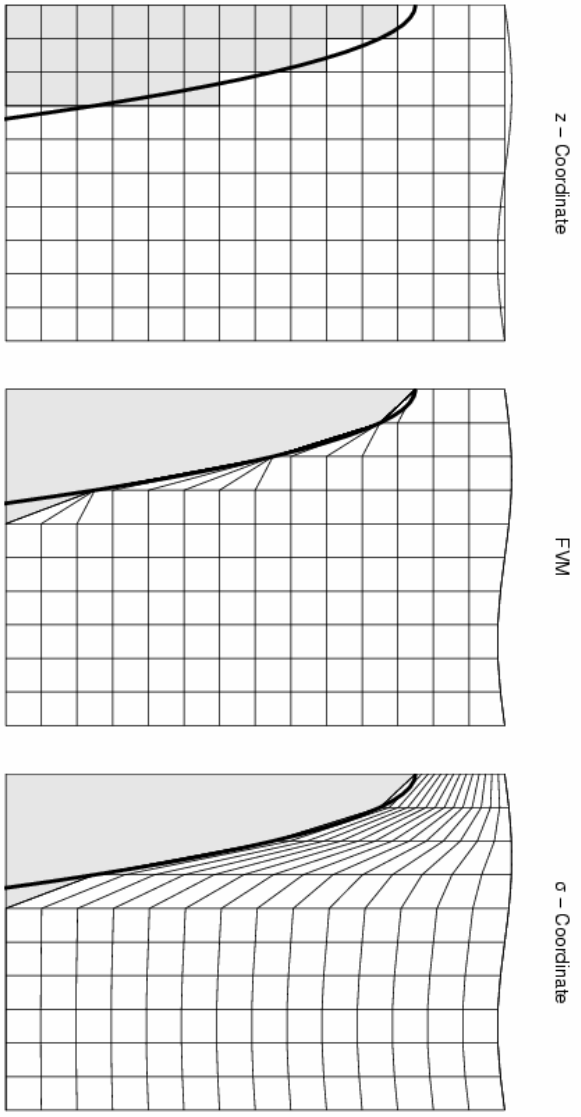

Fig. 2. Comparison among (a) *z*-coordinate, (b) finite volume, and (c) σ -coordinate systems.

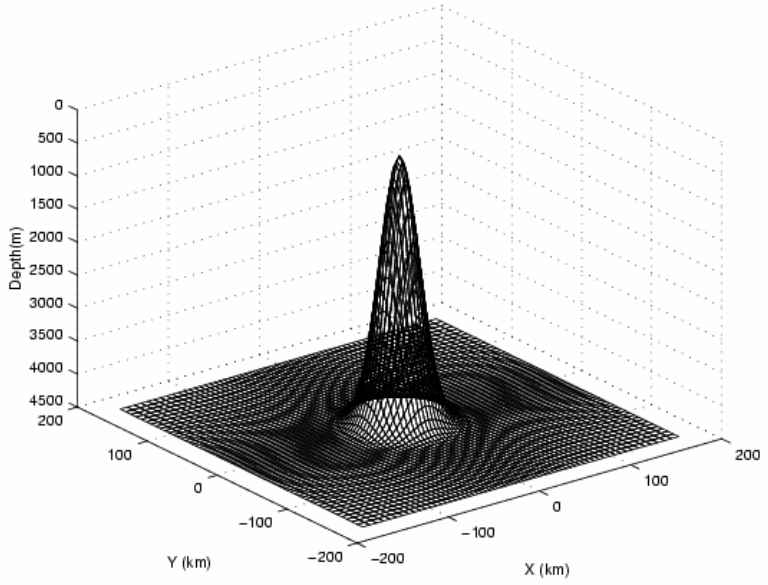

Fig. 3. Seamount geometry.

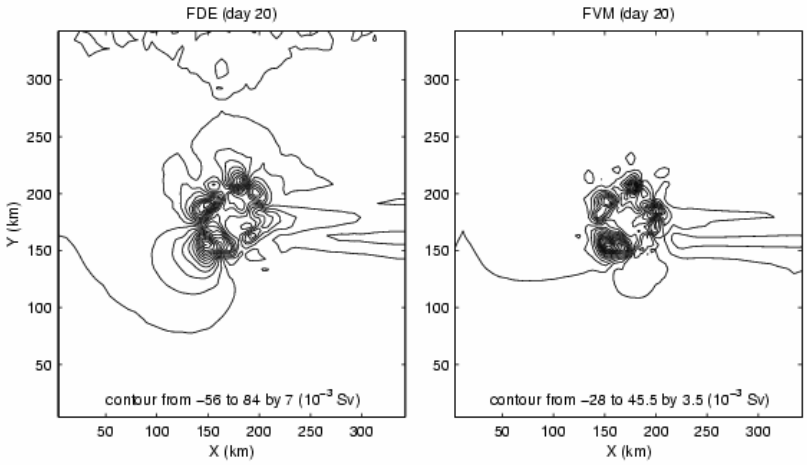

Fig. 4. Volume transport streamfunction (Sv) at day-20 using the finite difference and finite volume schemes.

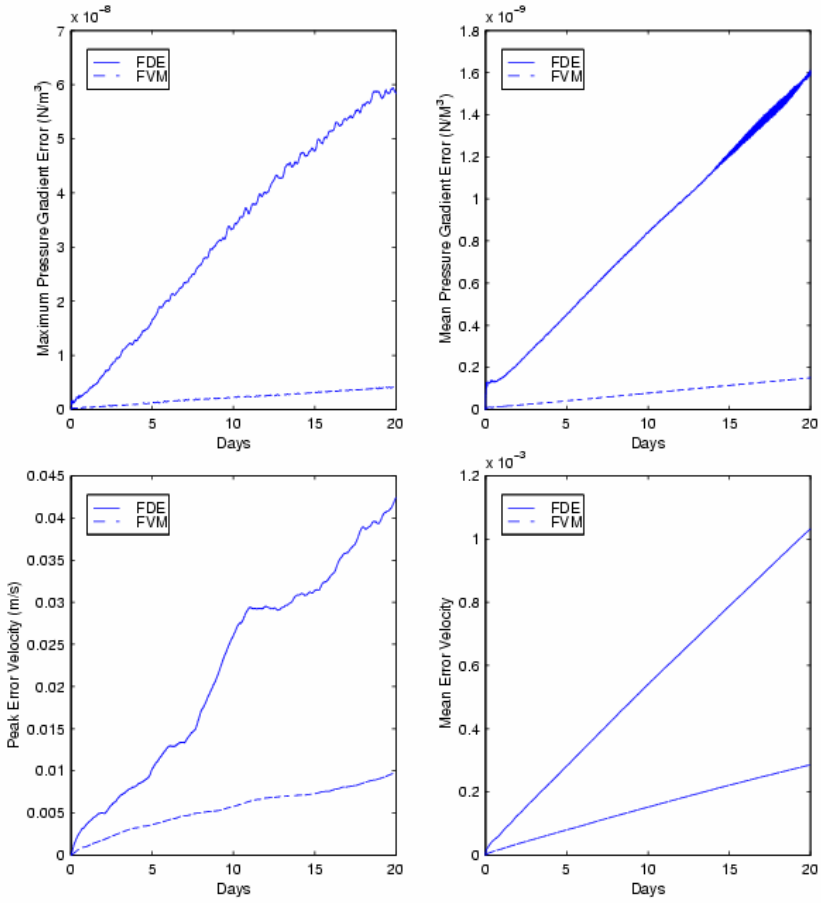

Fig. 5. Comparison between the finite difference and finite volume schemes on temporal variations of (a) maximum pressure gradient error (N/m^3), (b) mean pressure gradient error (N/m^3), (c) peak error velocity (m/s), and (d) mean error velocity (m/s).